

## Understanding strain localisation behaviour in a near- $\alpha$ Ti-alloy during initial loading below the yield stress

Claudius Dichtl<sup>1</sup>, David Lunt<sup>1</sup>, Rhys Thomas<sup>1</sup>, Michael Atkinson<sup>1</sup>, Matthew Thomas<sup>2</sup>, Dave Rugg<sup>3</sup>, Rebecca Sandala<sup>3</sup>, Joao Quinta da Fonseca<sup>1</sup>, Michael Preuss<sup>1</sup>

<sup>1</sup> University of Manchester, Manchester, M13 9PL

<sup>2</sup> TIMET UK, PO Box 704, Witton, B6 7UR

<sup>3</sup> Rolls-Royce plc, Derby, DE24 8BJ

### Highlights of this paper:

1. Observation of shear-bands at macroscopic loads as low as 70% of yield-stress
2. Material with coarse transformation product accumulate more plastic strain at same relative stress level than material with fine transformation product
3. At low stress levels average strains were identical for materials with different prior  $\beta$ -grain morphology, but differences can be observed for the maximum strain values and strain distribution
4. Even at low stress levels slip can be observed in primary  $\alpha$ , as well as in transformed- $\beta$  grains

### Abstract

Near- $\alpha$  Ti-alloys such as TIMETAL® 834 are known for their superior mechanical properties at high temperature, and as such are found in applications where high strength and improved fatigue performance at

elevated temperatures ( $>450^{\circ}\text{C}$ ) are required. However, these alloys can be susceptible to cold-dwell fatigue; a failure mechanism that is not well understood. The present work investigates the strain localisation behaviour during cold creep and the implications it has in terms of dwell susceptibility for two different bi-modal microstructures. Slip traces and strain distributions have been analysed for different material conditions by employing High-Resolution Digital Image Correlation (HRDIC) in combination with orientation mapping. Using this approach, it was possible to distinguish deformation patterns in primary  $\alpha$  grains and transformed- $\beta$  colonies, loaded incrementally to stress levels of 70%, 80% and 90% of the yield stress. Different prior  $\beta$ -grain morphologies didn't affect the average strains when stresses are low; but strain distributions have been affected by the  $\beta$ -grain morphology. Material with coarse transformation product accumulated larger amounts of plastic strain compared to material with fine transformation product, at the same relative stress levels. At low stress levels, slip bands have been detected both in primary  $\alpha$ , as well in the transformed- $\beta$  phase, cutting through the lamellae, for the material condition with a coarse transformation product; on the other hand, for the material conditions with a fine transformation product, slip bands are localised only in primary  $\alpha$  grains at low stress levels. It was also found for both conditions that at low stress levels slip bands are found in grains that are well oriented for basal slip. Based on these observations it is discussed if b-ligaments are significant obstacles to dislocation movement. Finally, the requirement of crystal-plasticity modelling to take into account differences in crystallographic orientations and the elastic and plastic anisotropy of HCP-titanium will be discussed and considered.

## 1 Introduction

Titanium alloys are often used in high performance applications, such as aerospace components, due to their high specific strength, fracture toughness and corrosion resistance. However, it has frequently been reported that titanium alloys exhibit cold creep at low temperature ( $T/T_m < 0.2$  [1]) and stresses well below the yield strength [2], [3]. Cold creep in titanium is commonly explained by either a high strain rate sensitivity [4] or interface sliding [5], [6].

In titanium alloys solution treated in the high  $\alpha+\beta$  phase regime the lamellar spacing of secondary  $\alpha$ , i.e. the transformation product, depends on the cooling rates. This means that high cooling rates results in high tensile strength due to reduced slip lengths in secondary  $\alpha$  [7]. It has been found that when the Burgers Orientation relationship between the secondary  $\alpha$  and the retained- $\beta$  is valid, dislocations might easily cut through the colony at least for one of the three possible  $\langle\alpha\rangle$  Burgers directions in the  $\alpha$ -phase. However, with

further misorientation from it,  $\alpha/\beta$  boundaries become a strong obstacle for dislocation movement [1], [8], [9].

Plastic deformation in titanium alloys is accommodated by dislocation movement in five distinct groups of slip systems: basal slip, prismatic slip and first order pyramidal slip with  $\langle a \rangle$ -type Burger's vector, and additionally first and second order pyramidal slip with  $\langle c+a \rangle$ -type Burger's vector [10]. The critically resolved shear stress at room temperature for  $\langle c+a \rangle$ -type slip is more than two times higher than for basal and prismatic slip with  $\langle a \rangle$ -type Burger's vector [7]. Bridier et al. showed that the active slip systems during tensile testing of Ti-6Al-4V are basal, prismatic and first-order pyramidal slip [10]. For stress levels below the yield-stress, basal and prismatic slip are the dominant slip systems [11], with basal slip being activated at the lowest stress levels [11], [12]. While this applies for lower stresses, at higher stresses pyramidal and prismatic slip are dominantly contributing to strain-localisation [13].

In a previous study, High-Resolution Digital Image Correlation (HRDIC) was used to show and analyse the formation of slip-bands in the  $\alpha+\beta$  titanium alloy Ti-6Al-4V for stresses below the yield point. McLean et al. focused on the effect of micro-textured regions in equiaxed microstructures on the strain-localisation behaviour [13]. It was found that pyramidal  $\langle c+a \rangle$  slip can be activated at low stress in micro textured regions with basal normal preferentially orientated in the loading direction, but that the formation of long bands of localised strain were formed by prismatic slip. In the present study we carry out a similar study on the titanium alloy TIMETAL-834 with a bi-modal microstructure. We use two billets with different thermo-mechanical processing history (Material A & B) and two different transformation products to study the effect of microstructure on the strain localisation. At first two materials nominally identified as A & B, both with fine transformation product, were analysed to study the effect of prior  $\beta$ -grain morphology. Then two conditions of Material B with different transformation products were tested to study the effect of cooling rate and lamella width. HRDIC analysis of images obtained in-situ during mechanical testing was used to probe the differences in mechanical response between primary  $\alpha$  grains and secondary  $\alpha$  colonies.

## 2 Experimental

### 2.1 Material

Two ingots of TIMETAL-834, with different forging histories were supplied by Titanium Metals Corporation (TIMET) UK. The two ingots have differences in the morphology of prior  $\beta$ -grains and are referred to as 'Material A' (smaller prior  $\beta$ -grains) and 'Material B' (larger prior  $\beta$ -grains). After forging, two different heat-treatments were applied to each material condition. The heat-treatments consisted of a 2 h solution-heat treatment at 1015 °C followed by cooling to room-temperature with either slow cooling (1 K/s) or fast cooling (10-30 K/s). The heat-treatment produces a bi-modal microstructure with either coarse (slow cooling) or fine (fast cooling) transformation product. Both conditions were subsequently annealed for 2 hours at 700 °C leading to the formation of  $\alpha_2$ -precipitates predominantly in the primary  $\alpha$  grains [14], [15].

### 2.2 Microstructure

The morphologies of the  $\beta$ -grains in near- $\alpha$  titanium alloys cannot be easily obtained by EBSD-based orientation mapping of the  $\beta$ -phase, as the volume fraction is low and the width of the  $\beta$ -lamellae is only around 0.1  $\mu\text{m}$ . Instead crystallographic orientation maps of  $\alpha$ -phase were recorded using EBSD from which the  $\beta$ -phase was reconstructed using an algorithm, based on the Burgers orientation relationship [16]. The material conditions with the fine transformation product were used for the comparison, as the secondary  $\alpha$  colonies are smaller, which has proven to result in a higher fraction of data points with successful  $\beta$ -reconstruction. Only one material condition for each Material A & B was analysed, as it is assumed that the  $\beta$ -morphology is not changed by the cooling rate or annealing heat treatment. For EBSD-mapping a TESCAN Mira3 field emission gun scanning electron microscope equipped with the Oxford Instrument-Symmetry detector was utilised. The beam settings were 20kV, 96 nA and a step size of 7.5  $\mu\text{m}$  was used.

Optical bright field microscopy was used to determine the volume fraction and size distribution of primary  $\alpha$  grains and the lamella spacing of the transformation product for all material conditions. Specimens were ground with abrasive paper (to 4000 grit), polished in a colloidal silica solution and then etched with Kroll's reagent (2 ml HF, 4 ml HNO<sub>3</sub>, 94 ml H<sub>2</sub>O) to reveal the underlying microstructure. The difference in

brightness of primary  $\alpha$  phase compared to transformed- $\beta$  phase was used to separate the two phases and create a binary image. The ‘Detect particle’ function in ‘Fiji’ was then utilised to determine the volume fraction of primary  $\alpha$ . The lamella spacing of secondary  $\alpha$  was determined by applying the line intersection method on 30 colonies.

### 2.3 Mechanical testing

For the mechanical baseline characterisation and HRDIC experiments, flat dog-bone specimens with a cross-section of  $3 \times 1 \text{ mm}^2$  were used. Uniaxial tensile testing was carried out on a Instron 5569 electromechanical tester at a constant strain-rate of  $0.005 \text{ 1/s}$  to record stress-strain curves and to determine the  $0.2\%$ -proof stress of each material condition [17]. The results are shown in **Table 2**.

HRDIC analysis requires a pattern of distinct features on the sample surface. Therefore the samples were ground and polished with colloidal silica. A thin layer of gold was deposited on the surface using a sputter-coater. The gold-layer was broken up and transformed to distinct nano-sized particles using water-vapour remodelling process at a temperature of  $275^\circ\text{C}$  for 2 hours [18].

The HRDIC experiments were carried out in-situ, using a ‘Deben’ 5kN tensile stage inside a ‘FEI-Quanta 650’ FEG-SEM. This allows the sample to be mechanically loaded during imaging. All mechanical loading is at stress levels relative to the  $0.2$  proof stress of each specimen. Three load steps were used:  $70$ ,  $80$  and  $90$  percent of the  $0.2\%$  proof stresses, referred to here as the yield stress ( $\sigma_y$ ). After being loaded to the first load step, the stress was held constant for 10 minutes to accommodate the plastic deformation. Then the load was reduced by  $5\%$ , e.g. from  $70\%$  of  $\sigma_y$  to  $65\%$  of  $\sigma_y$ , to stop any further deformation process. At this stress level the samples were imaged, before the next load steps were applied in the same way. The images were recorded at  $10 \text{ kV}$  and at working distance of  $11.7 \text{ mm}$  with  $2048$  pixels wide at a field width of  $30 \mu\text{m}$ . A mosaic of  $8 \times 8$  images were recorded, which were then stitched into a large image, using ‘Grid/Collection stitching’ plug-in for ‘Fiji’ [19], [20], resulting in a stitched imaged of  $180 \times 180 \mu\text{m}^2$ .

### 2.4. Processing of DIC data

Digital image correlation (DIC) was performed using LaVision DaVis 8.4.0 software. In DIC, the local displacements are determined by comparing the undeformed image to the deformed image at each load step. For the correlation process a sub-window size of  $24 \times 24$  pixels was used, resulting in a spatial resolution of  $350 \text{ nm}$ . As there is a variation in the morphology of the gold pattern between grains, some areas exhibit higher noise levels than others. To reduce noise, a Gaussian filter is applied to the strain data. The deformation maps consist of strain components parallel ( $\varepsilon_{xx}$ ) and perpendicular ( $\varepsilon_{yy}$ ) to the loading direction  $x$ , and a shear component ( $\varepsilon_{xy}$ ). From these three vectorial components the scalar  $\gamma_{eff}$  is calculated, which is referred to as the effective shear strain (1) [18], [21]. Effective shear strain is used as it takes all in-plane shear components into account.

$$\gamma_{eff} = \sqrt{\left(\frac{\varepsilon_{xx} - \varepsilon_{yy}}{2}\right)^2 + \varepsilon_{xy}^2} \quad (1)$$

To display slip-bands and overlay them on top of microstructural maps, areas of high strain are segmented in the strain maps. Due to low levels of strain and higher than usual experimental noise due to the in-situ set up, the noise level can be close to the strain values. Segmenting the strain data helps displaying deformation patterns without random noise. All data points in a strain map with strain values higher than a threshold value are accepted, while all other points are discarded. The threshold value is set to be the  $99^{\text{th}}$  percentile of the strain distribution, as noise and artefacts might also be segmented for lower threshold values. This segmentation results in a binary image of slip-bands, were the exact values within the slip-bands are lost.

To calculate the expected elastic effective shear strain, equation (1) is used along with an assumption of isotropic elastic behaviour. The Poisson-ratio is assumed to be  $0.3$ , Young’s modulus is determine to be  $117 \text{ GPa}$  from tensile testing, and the shear component  $\varepsilon_{xy}$  needs to be set to zero.

## 3 Results

In **Fig.1** the  $\beta$ -phase morphology of Material A and Material B is displayed. Material A exhibits what seem to be small b grains, but in some cases there are areas with common crystallographic orientation that are several millimetres in size. While there appears to be a preferential orientation within each area, there are also other orientations present. The boundaries are diffuse, making it difficult to define a clear prior  $\beta$ -grain size. In contrast, Material B exhibits grains with a size of up to 500  $\mu\text{m}$ , which only have one crystallographic orientation and a clear boundary. These clearly defined grains are separated from each other by regions with randomised texture. Overall, Material A exhibits smaller b grains, but there are very long chains of very similarly orientated b-grains. The  $\beta$ -grains in Material B are larger than individual b-grains in Material A but smaller and with sharper outlines compared to the areas of similarly orientated b-grains in Material A.

The primary  $\alpha$  grain size, primary  $\alpha$  volume fraction and lamella spacing are calculated from the optical images provided in **Fig.2** and summarised in **Table 1**. For Material A & B, the fast cooling rate results in similar lamella spacing of just over 1  $\mu\text{m}$ . While the primary  $\alpha$  volume fraction is similar for both materials, Material B exhibits a smaller average primary  $\alpha$  grain size; a difference which originates from differences in the initial thermomechanical processing route. Comparing different cooling rates for Material B reveals that slower cooling results in the lamella spacing being approximately 60 % wider than for the faster cooling rate. The slower cooled material condition with coarse transformation product also has a higher primary  $\alpha$  volume fraction (23 %) compared to the faster cooled, finer transformation product (18 %). This variation is due to the slower cooling rate giving more time for grain growth [22].

The average strain values for each material condition are summarised in **Table 2** and plotted in **Fig.3**. At first a comparison is made between Material A & B, both in a material condition with fine lamella spacing. As both materials have similar yield strength (see Table 2), the applied stresses are almost identical. At 70 and 80 % of  $\sigma_Y$  the two materials exhibit similar effective shear strain approximately 0.2 % higher than the expected elastic strain but with a similar slope to the elastic response (**Fig. 3, b**). It is therefore concluded that the increase in strain from the first to the second load step is mainly elastic, a little additional plastic strain is accumulated in the samples (0.2 %). From 80 to 90 % of  $\sigma_Y$  load step, the strain increases two times more for Material A – fine lamella (increase of ~0.8 %) compared to Material B – fine lamella (increase of ~0.3 %). An increase that must be attributed to differences in the  $\beta$ -phase morphology.

Next samples with coarse and fine transformation product (both Material B) are compared. At the 70 % of  $\sigma_Y$  load step, both material condition exhibit similar average effective shear strain (**Fig. 3, a**). As the material with coarse secondary  $\alpha$  lamella has a lower strength, it has been tested at lower applied stresses. This can be seen by the curve of Material B – coarse lamella being shifted to lower stress values when plotted as a function of stress (**Fig. 3 b**). At 80 and 90 % of  $\sigma_Y$  strain accumulates more for the material with coarse lamella; at 90 % of  $\sigma_Y$ , the strain is double the effective shear strain of the fine lamella material.

In **Fig. 4**, frequency distributions of the effective shear strain at 70 % of  $\sigma_Y$  are plotted for comparing **a)** Material A & B fine lamella and **b)** Material B with fine and coarse lamella. To highlight variations, the effective shear strain is normalized by the average effective shear strain. Comparing Material A & B – fine lamella with each other shows that for normalised shear strain values lower than 2, both curves are almost completely identical. Also the values of the 99<sup>th</sup> percentile of the strain distribution are close together for both materials. But for values higher than 2, significant differences between both samples are observed. For Material B the highest effective shear strain values are approximately 3.5 times higher than the average value. For Material A they are more than twice as high, with values of up to 8 times the average strain. This indicates that in Material A the strain distribution is more heterogeneous and that slip bands with higher strain values are formed. This comparison indicates that  $\beta$ -phase morphology impacts the heterogeneity of strain, however, since the frequency of the strain values higher than two times the average is low, the high strain values only have a small impact on the average strain.

Similar observations are made comparing Material B with coarse and fine lamella (**Fig. 4b**). The strain distributions look similar below 1.5 times the average effective shear strain. For values above this range, the frequency is up to one order of magnitude higher for the material with coarse lamella. Also the maximum effective shear strain values of Material B – coarse lamella is around 65 % higher than for Material B – fine lamella. As higher frequency of high strain values has been observed at the same average strain, the strain distribution of the material with coarse lamella is more heterogeneous.

**Fig. 5** shows a skeleton map of average Schmid factor for basal slip overlaid with the 99<sup>th</sup> percentile of effective shear strain at 70% of  $\sigma_Y$  for all conditions. Basal slip is chosen, as it is assumed to be the slip

system that is activated at the lowest stress levels [10]. For all conditions, the high strain slip bands are all in grains with a Schmid factor >0.3. This indicates the dominant active slip system is likely to be basal slip. It should be noted that without more detailed Burgers vector analysis this is only a qualitative assessment of slip activity. The frequency distributions of the Schmid factors for basal and prismatic slip (**Fig. 6**) show similar distributions for both slip systems. Hence, based on the crystallographic orientations and the Schmid factors, the activation of both slip systems seems to be equally likely. For Material A – fine lamella and Material B – coarse lamella, well defined slip bands, 25 to 50  $\mu\text{m}$  long can be observed. These are the two material conditions that exhibit higher strain values than Material B – fine lamella; relative to their average strain values (see **Fig. 4**). In contrast, for Material B – fine lamella the slip bands are shorter.

**Fig. 7** shows the effective shear strain values higher than the 99<sup>th</sup> percentile (for the 70 % of  $\sigma_Y$  load step) overlaid in red on top of backscattered electron images of the microstructures for Material B with both fine and coarse lamella. The sample with the coarser transformation product exhibits high strain slip-bands in both primary  $\alpha$  and secondary  $\alpha$  colonies, where the slip bands in the secondary  $\alpha$  colonies are cutting across the lamellae. Conversely, slip-bands are only observed in the primary  $\alpha$  grains for the material with the finer transformation product.

### 3. Discussion

The morphology of prior  $\beta$ -grain structure has been analysed for two materials. Material A exhibits large areas of similarly orientated  $\beta$  grains reaching several mm in size. In Material B the  $\beta$ -grains are better defined and sharper, but smaller (less than 1 mm) than the similar orientated  $\beta$ -grain regions for material A. At low stress levels (70 and 80 % of  $\sigma_Y$ ) the average strain values did not reveal any difference between materials A & B. Only at a stress level of 90% of  $\sigma_Y$  Material A exhibits higher strain values than Material B. But even at low applied stress (70% of  $\sigma_Y$ ) a few events of much higher shear strain values can be found in Material A, leading to a more heterogeneous strain distribution.

When comparing material with fine and coarse transformation product, it was shown that material with coarse lamella was accumulating more plastic deformation at the same relative stress levels than material with fine lamella. Also, the strain distribution is more heterogeneous for material with coarse lamella. As the yield stress is lower for material with coarse lamella, the same relative stress levels correlate to a lower applied stresses.

Slip-bands can be seen in all material conditions even at 70% of  $\sigma_Y$ , but the small number of slip-bands only has a small effect on the average strain. At lower strain levels, noise and measuring artefacts can influence the results, making it harder to interpret differences between samples. Therefore segmented strain maps have been displayed, which show the high strain regions and allow removing noise.

The correlation of HRDIC results with crystallographic orientation data showed that at 70 % of  $\sigma_Y$ , all observed strain higher than the 99<sup>th</sup> PCTL were located in grains well aligned for basal slip. Although this alone is not confirmation of the activated slip system, the observation aligns with results in literature that basal slip is activated at the lowest stresses. In future work, ‘relative displacement ratio’ (RDR) technique will be used to unambiguously determine the activated slip system.

The difference in strength between fine and coarse  $\beta$ -transformation product correlates with the strain localization behaviour. For the material with coarse transformation product slip bands can be found in both phases, suggesting there is no difference in strength between primary  $\alpha$  and transformed  $\beta$ . In the secondary  $\alpha$  colonies, slip bands cut through the lamellae in the transformed  $\beta$ -phase. In the material with the finer transformation product, no strain above the 99<sup>th</sup> percentile has been observed in secondary  $\alpha$  colonies. This is in agreement with the assumption that finer transformation product has a more pronounced strengthening effect [7]. However these observations cannot prove that there are no slip-bands in the transformed- $\beta$  phase, as the observed areas are not large enough and as strains below the 99<sup>th</sup> percentile were not considered.

The analysed samples are very similar in texture on a macroscopic scale, however there are variations in local texture which, in combination with the elastic anisotropy of titanium, might have effects on local average

strains and strain distributions. Crystal-plasticity modelling is required to take the effects of local texture and elastic and plastic anisotropy into account.

## 5 Conclusions

- For all material conditions slip bands have been observed at 70% of yield stress
- Regarding average strain values materials with different prior  $\beta$ -grain structure performed identically at low stress levels
- Material with large but diffuse prior  $\beta$ -grains accumulates more plastic strain than material with small and sharp prior- $\beta$  grains for stresses close to the yield point
- Material with large prior  $\beta$ -grains exhibits higher strain values and more heterogeneous strain distribution for low stresses
- At low stress level slip can be observed in primary  $\alpha$ , as well as in transformed  $\beta$ -phase for material with coarse transformation product
- For material with fine transformation product, slip bands are only observed in primary  $\alpha$  grains

## Acknowledgement

The authors would like to thank the EPSRC funding the project through the CDT in Advanced Metallic Systems. The authors would also like to thank Rolls-Royce plc and TIMET for providing additional funding and the provision of material.

## Reference

- [1] S. Suri, G. B. Viswanathan, T. Neeraj, D.-H. Hou, and M. J. Mills, "Room temperature deformation and mechanisms of slip transmission in oriented single-colony crystals of an  $\alpha/\beta$  titanium alloy," *Acta Mater.*, vol. 47, no. 3, pp. 1019–1034, 1999.
- [2] S. Suri, T. Neeraj, G. S. Daehn, D.-H. Hou, J. M. Scott, R. W. Hayes, and M. J. Mills, "Mechanisms of primary creep in  $\alpha/\beta$  titanium alloys at lower temperatures," *Mater. Sci. Eng. A*, vol. 234–236, pp. 996–999, Aug. 1997.
- [3] M. A. Imam and C. M. Gilmore, "Room temperature creep of Ti-6Al-4V," *Metall. Trans. A*, vol. 10, no. 4, pp. 419–425, 1979.
- [4] B. C. Odegard and A. W. Thompson, "Low temperature creep of Ti-6 Al-4 V," *Metall. Trans.*, vol. 5, no. 5, pp. 1207–1213, 1974.
- [5] W. H. Miller, R. T. Chen, and E. A. Starke, "Microstructure, creep, and tensile deformation in Ti-6Al-2Nb-1Ta-0.8 Mo," *Metall. Trans. A*, vol. 18, no. August, pp. 1451–1468, 1987.
- [6] S. Ankem and H. Margolin, "A rationalization of stress-strain behavior of two-ductile phase alloys," *Metall. Trans. A*, vol. 17, no. 12, pp. 2209–2226, 1986.
- [7] G. Lütjering and J. C. Williams, "Titanium: Engineering Materials and Processes," *Ed. Springer*, vol. second edi, pp. 1–442, 2007.
- [8] D. Qiu, R. Shi, D. Zhang, W. Lu, and Y. Wang, "Variant selection by dislocations during  $\alpha$  precipitation in  $\alpha/\beta$  titanium alloys," *Acta Mater.*, vol. 88, pp. 218–231, 2015.
- [9] D. He, J. Zhu, S. Zaefferer, and D. Raabe, "Effect of retained beta layer on slip transmission in Ti-6Al-2Zr-1Mo-1V near alpha titanium alloy during tensile deformation at room temperature," *Mater.*

Des., vol. 56, pp. 937–942, Apr. 2014.

- [10] F. Bridier, P. Villechaise, and J. Mendez, “Analysis of the different slip systems activated by tension in a  $\alpha/\beta$  titanium alloy in relation with local crystallographic orientation,” *Acta Mater.*, vol. 53, no. 3, pp. 555–567, 2005.
- [11] S. Hémery and P. Villechaise, “Comparison of slip system activation in Ti-6Al-2Sn-4Zr-2Mo and Ti-6Al-2Sn-4Zr-6Mo under tensile, fatigue and dwell-fatigue loadings,” *Mater. Sci. Eng. A*, vol. 697, pp. 177–183, Jun. 2017.
- [12] S. Hémery, V. T. Dang, L. Signor, and P. Villechaise, “Influence of Microtexture on Early Plastic Slip Activity in Ti-6Al-4V Polycrystals,” *Metall. Mater. Trans. A*, vol. 49, no. 6, pp. 2048–2056, Jun. 2018.
- [13] M. P. Echlin, J. C. Stinville, V. M. Miller, W. C. Lenthe, and T. M. Pollock, “Incipient slip and long range plastic strain localization in microtextured Ti-6Al-4V titanium,” *Acta Mater.*, vol. 114, pp. 164–175, Aug. 2016.
- [14] K. V. S. a I. Srinadh, N. Singh, and V. Singh, “Role of Ti<sub>3</sub>Al / silicides on tensile properties of Timetal 834 at various temperatures,” *Bull. Mater. Sci.*, vol. 30, no. 6, pp. 595–600, 2007.
- [15] A. Radecka, J. Coakley, V. A. Vorontsov, T. L. Martin, P. A. J. Bagot, M. P. Moody, D. Rugg, and D. Dye, “Precipitation of the ordered  $\alpha_2$  phase in a near- $\alpha$  titanium alloy,” *Scr. Mater.*, vol. 117, pp. 81–85, 2016.
- [16] P. S. Davies, “An investigation of microstructure and texture evolution in the near-alpha Titanium alloy Timetal 834,” The University of Sheffield, 2009.
- [17] ASTM Int., “Standard Test Methods for Tension Testing of Metallic Materials 1,” *Astm*, no. C, pp. 1–27, 2009.
- [18] F. Di Gioacchino and J. Quinta da Fonseca, “Plastic Strain Mapping with Sub-micron Resolution Using Digital Image Correlation,” *Exp. Mech.*, vol. 53, no. 5, pp. 743–754, 2013.
- [19] P. Tomancak, S. Preibisch, and S. Saalfeld, “Globally optimal stitching of tiled 3D microscopic image acquisitions,” *Bioinformatics*, vol. 25, no. 11, pp. 1463–1465, 2009.
- [20] J. Schindelin, I. Arganda-Carreras, E. Frise, V. Kaynig, M. Longair, T. Pietzsch, S. Preibisch, C. Rueden, S. Saalfeld, B. Schmid, J.-Y. Tinevez, D. J. White, V. Hartenstein, K. Eliceiri, P. Tomancak, and A. Cardona, “Fiji: an open-source platform for biological-image analysis,” *Nat. Methods*, vol. 9, p. 676, Jun. 2012.
- [21] T. Goswami, “Low cycle fatigue—dwell effects and damage mechanisms,” *Int. J. Fatigue*, vol. 21, no. 1, pp. 55–76, 1999.
- [22] O. N. Senkov, J. J. Valencia, S. V. Senkova, M. Cavusoglu, and F. H. Froes, “Effect of cooling rate on microstructure of Ti-6Al-4V forging,” *Mater. Sci. Technol.*, vol. 18, no. 12, pp. 1471–1478, 2002.

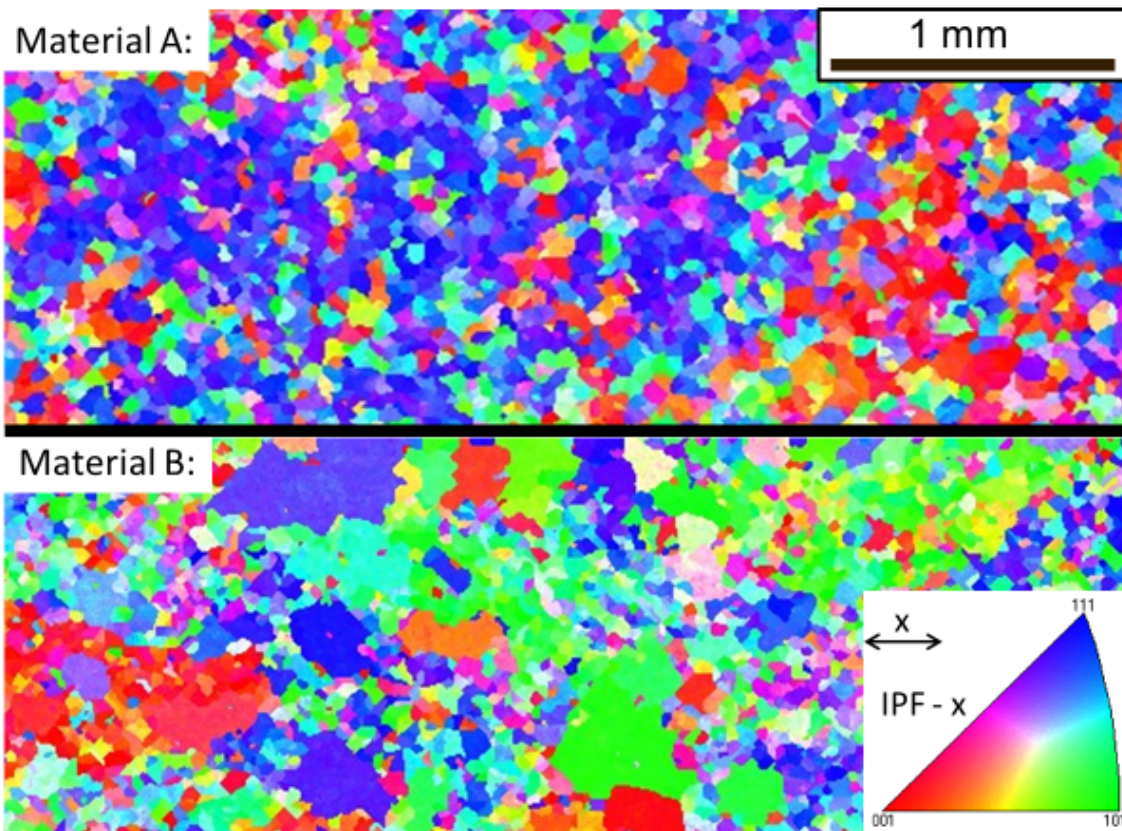


**Figure 1:** Crystallographic orientation maps of  $\beta$ -phase for two material conditions A & B. The IPF-colouring is displayed for the reference direction 'X', which is in parallel to the loading direction. The maps have been created from EBSD-data of  $\alpha$ -phase using reconstruction algorithm.

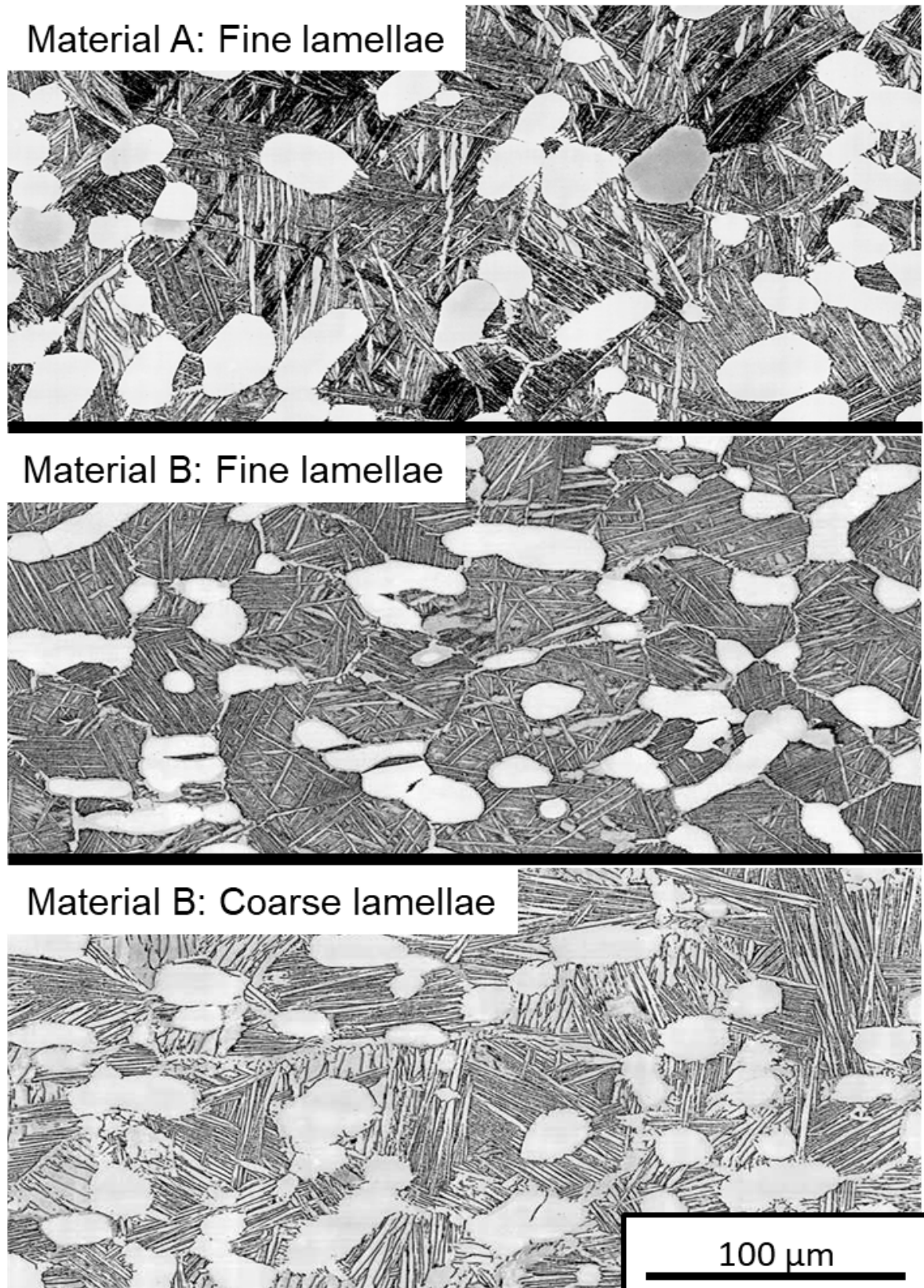


Figure 2: Optical micrographs of etched specimens for three material conditions, showing the morphology of primary  $\alpha$  grains and secondary  $\alpha/\beta$  lamellae.

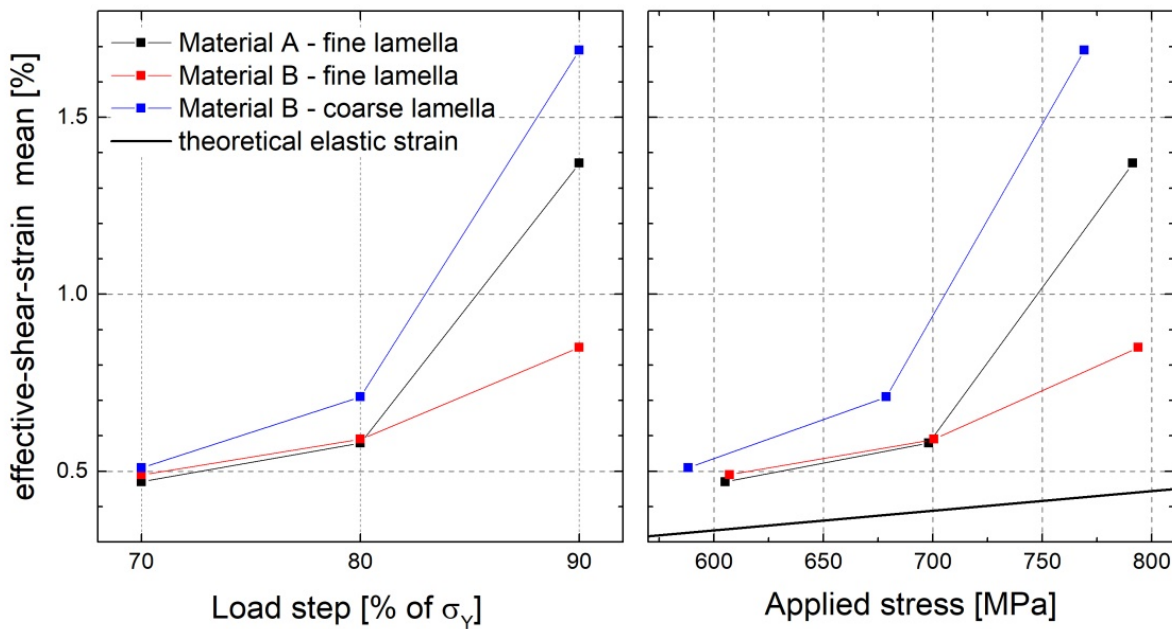


Figure 3: The mean effective shear strain for each load step and material condition is plotted as function of a) load step and b) applied stress. The stresses in b) refer to 65, 75 and 85 % of  $\sigma_Y$ , which are the stress levels at which the strain maps have been recorded. The black line in plot b) shows the theoretical elastic response of the material.

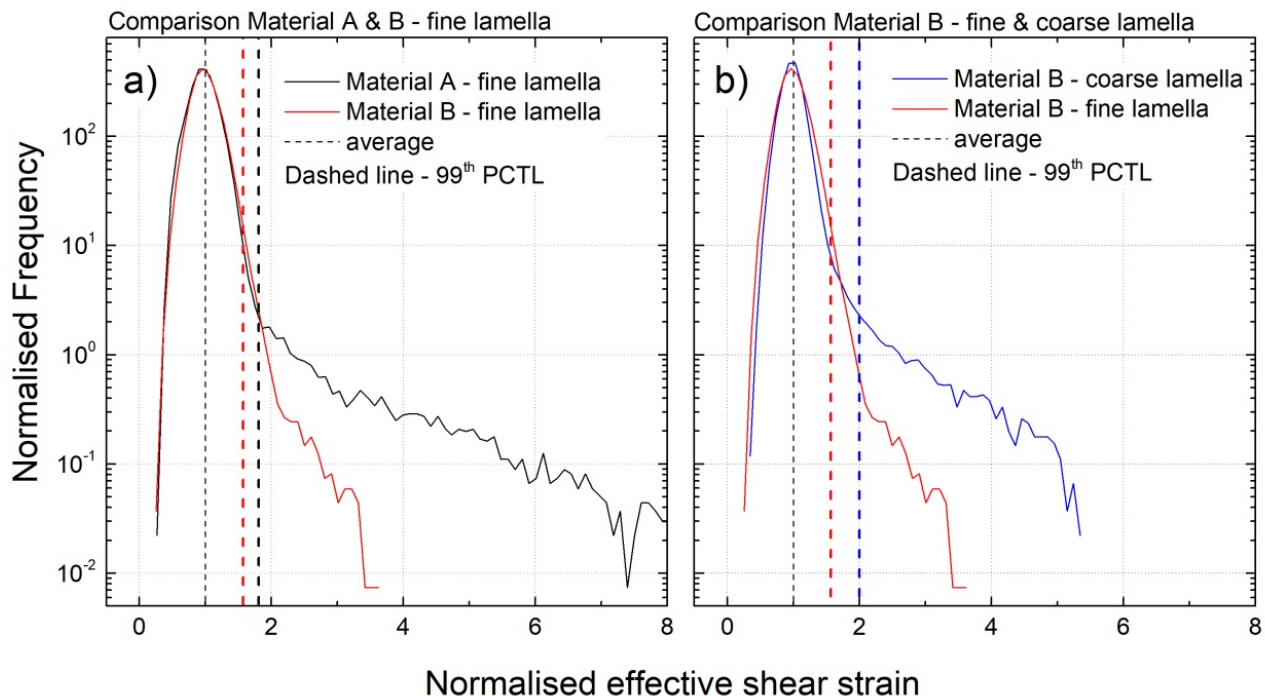


Figure 4: Normalised frequency distribution of the effective shear strain at 70% of  $\sigma_Y$ , comparing a) Material A & B both with fine lamella and comparing b) coarse and fine lamella for Material B. The dashed lines show the normalised 99th PCTL for each material condition.

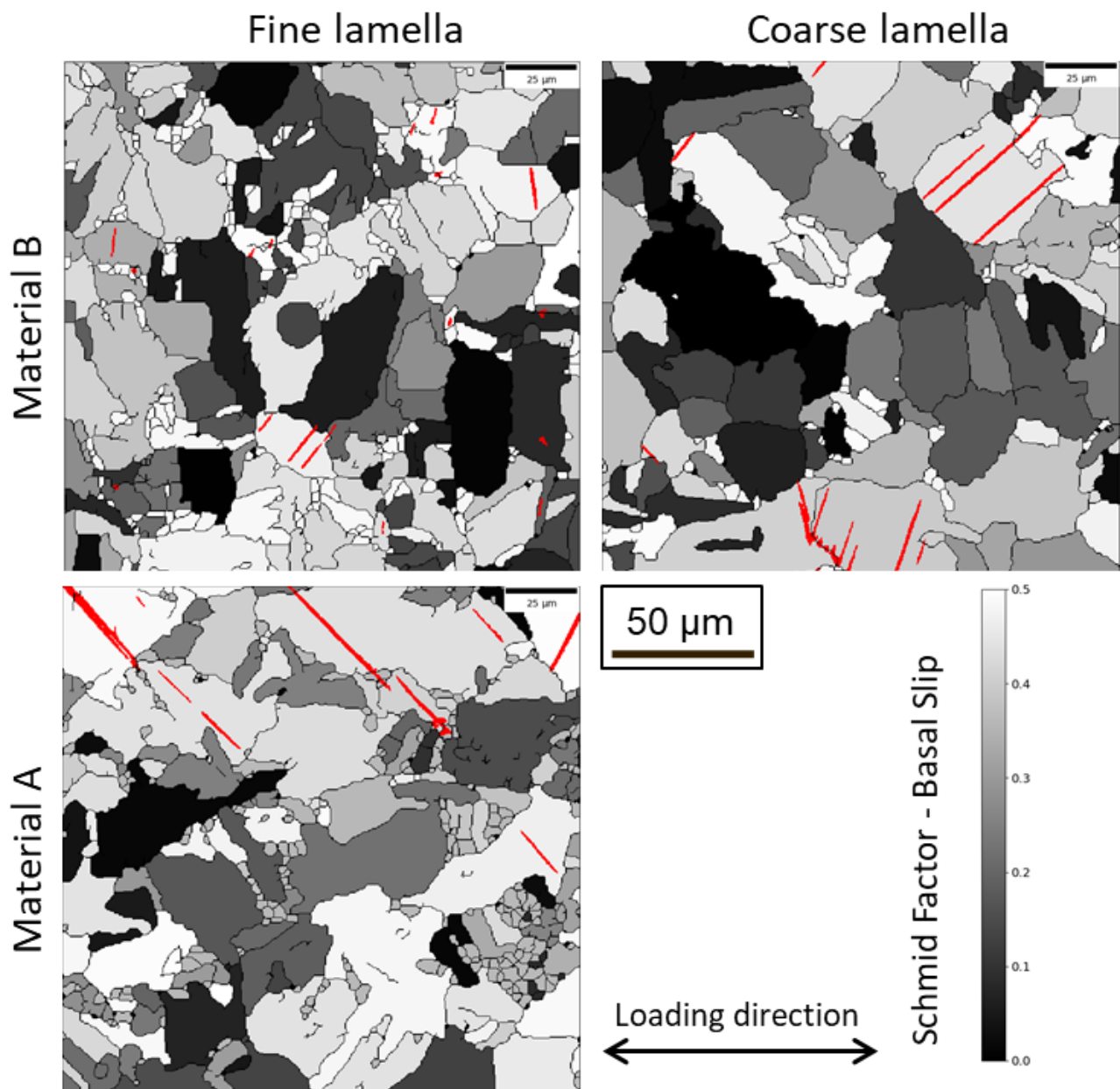


Figure 5: The 99th PCTL of the effective shear strain is used for segmenting the strain maps of the 70% of  $\sigma_Y$  load step. The values for each material for the 99th PCTL are given in Table 2. Areas with strain values above this threshold are displayed in red. The strain data is displayed on top of Schmid-factor maps for basal slip.

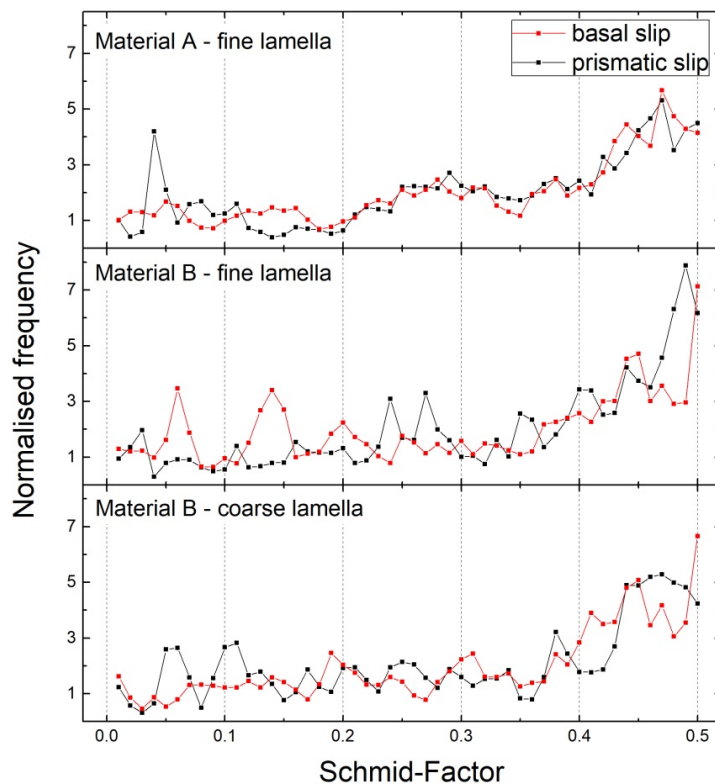


Figure 6: Frequency distributions of Schmid factors of basal and prismatic slip.

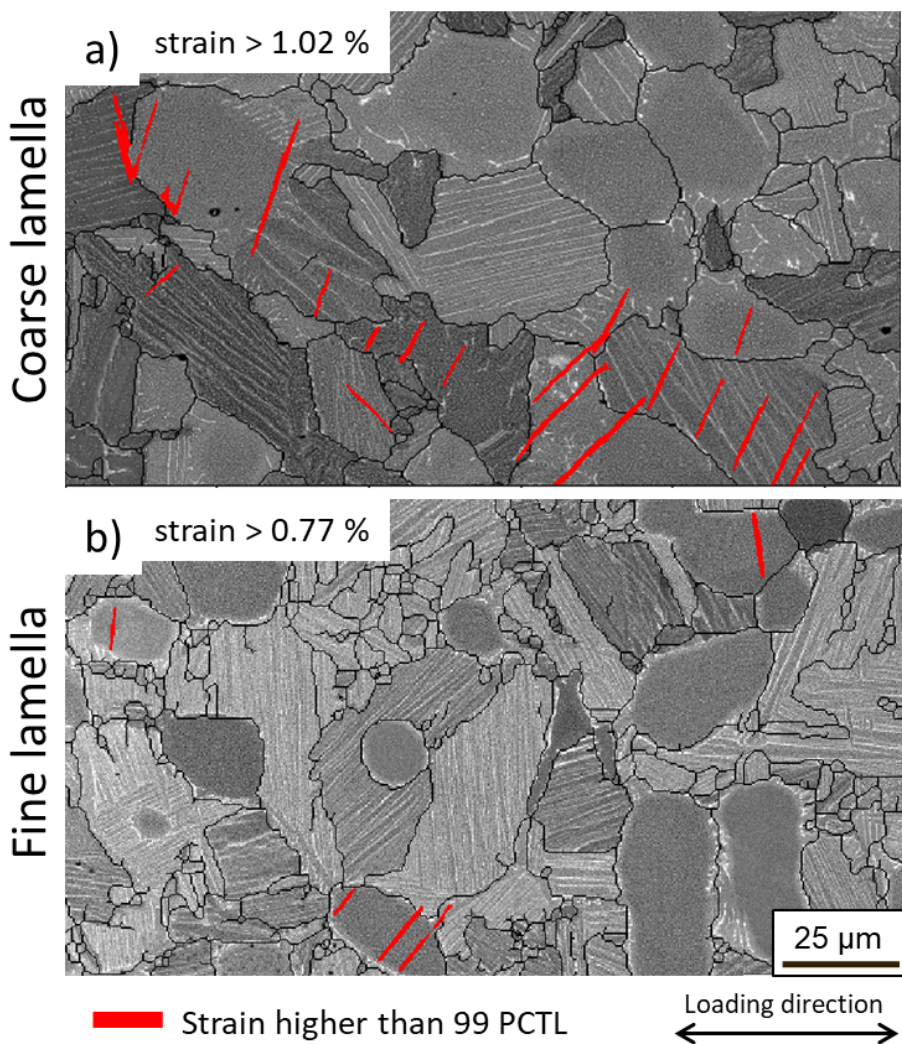


Figure 7: Areas with strain values above the 99 PCTL are displayed in red. The strain data is displayed on top of BSE-image showing the microstructure of the material condition with a) coarse and b) fine transformation product for Material B. Black lines are showing grain boundaries with misorientation of 10°.

Table 1: Summary of microstructure analysis based on micrographs displayed in Fig. 2

	<b>Material A</b>		<b>Material B</b>	
	Fine lamellae	Fine lamellae	Coarse lamellae	Coarse lamellae
<b>Lamella spacing</b>	$1.2 \pm 0.1 \mu\text{m}$	$1.1 \pm 0.3 \mu\text{m}$	$1.8 \pm 0.4 \mu\text{m}$	
<b>Primary <math>\alpha</math> Volume fraction</b>	$19.7 \pm 0.7 \%$	$18.2 \pm 1.0 \%$	$23.1 \pm 0.3 \%$	
<b>Average <math>\alpha(P)</math> grain size (area)</b>	$506 \pm 9 \mu\text{m}^2$	$379 \pm 18 \mu\text{m}^2$	$469 \pm 11 \mu\text{m}^2$	

Table 2: Loading conditions and results of mechanical testing and HR-DIC testing. Mean value and 99th percentile (PCTL) of effective shear strain are determined for complete deformation maps.

	Transformation product	Yield stress $\sigma_y$ [%]	Load step [% of $\sigma_y$ ]	Load step [MPa]	Effective shear strain [%]	
					Mean	99th PCTL
Material A	Fine	931	70	652	0.47	0.85
			80	745	0.58	2.07
			90	838	1.37	6.33
Material B	Fine	934	70	654	0.49	0.77
			80	747	0.59	1.06
			90	841	0.85	2.89
	Coarse	905	70	634	0.51	1.02
			80	724	0.71	2.51
			90	815	1.69	7.06